infrastructures

MDPI

Article

Numerical Investigation of the Seismic Performance of FRP-Reinforced Tunnel Linings Under Dynamic Excitation

Qiwei Lin, Yujing Jiang * and Satoshi Sugimoto

Graduate School of Engineering, Nagasaki University, Nagasaki 852-8521, Japan; linqiweilinki@163.com (Q.L.)
* Correspondence: bb52223107@ms.nagasaki-u.ac.jp

Abstract

Tunnel linings are critical structural components of underground infrastructure, and their seismic performance plays a decisive role in maintaining the serviceability and safety of tunnels. Under dynamic loading, excessive deformation and damage of the lining may reduce the effective cross-sectional capacity and threaten the minimum safety clearance required for tunnel operation. Therefore, it is essential to investigate the deformation behavior and failure mechanisms of tunnel linings subjected to seismic excitation and to evaluate the effectiveness of reinforcement measures. In this study, a coupled numerical framework combining the finite difference method (FLAC3D) and the discrete element method (PFC3D) is developed to analyze the dynamic response of tunnel lining systems. The surrounding rock mass is modeled in FLAC3D to simulate stress wave propagation and global deformation, while the tunnel lining is represented in PFC3D using bonded particles to capture crack initiation, propagation, and post-peak failure behavior. The proposed FLAC3D–PFC3D coupled approach provides an effective tool for evaluating the seismic performance of reinforced tunnel linings and offers a practical basis for the design and assessment of seismic strengthening measures in underground engineering.

Keywords: tunnel lining; seismic response; displacement; FLAC3D–PFC3D coupling; FRP reinforcement

1. Introduction

Tunnel structures constitute an essential component of modern transportation infrastructure and are expected to maintain long-term operational safety under both static and dynamic loading conditions. In seismically active regions, tunnels are frequently subjected to ground shaking, which may induce significant deformation, cracking, and local damage in tunnel linings. Excessive displacement of the lining can reduce the effective clearance of the tunnel and threaten the minimum safety cross-section required for safe operation, making deformation control a critical concern in seismic tunnel engineering. Seismic events can cause various forms of tunnel damage, including invert uplift, lining cracking, shear failure, and even partial collapse, highlighting the vulnerability of tunnel linings under dynamic loading (Figure 1).

Check for updates

Academic Editors: Yulong Shao, Jingwei Yang and Chen He

Received: 13 February 2026
Revised: 4 March 2026
Accepted: 9 March 2026
Published: 17 March 2026

Figure 1. Diverse seismic damage modes (invert uplift, lining collapse, lining crack, shear failure of lining) reproduced from Damage Analysis of Tunnels during the 2024 Noto Peninsula Earthquake, Ministry of Land, Infrastructure, Transport and Tourism (MLIT), 2024 [1].

To better understand the dynamic behavior of underground structures, numerical modeling has become an indispensable tool. Continuum-based methods, such as the finite difference method implemented in FLAC3D, are effective in simulating stress redistribution and wave propagation in large-scale rock masses. Recent advances in numerical modeling have significantly improved the understanding of tunnel–rock interaction under dynamic loading. Continuum-based approaches, such as the finite difference method implemented in FLAC3D, are widely used to simulate large-scale deformation, stress redistribution, and seismic wave propagation in rock masses. Nevertheless, Carranza-Torres and Fairhurst (1999) and Ju et al. (2019) demonstrated that continuum models have inherent limitations in capturing localized fracture processes, contact separation, and post-peak failure behavior of structural materials [2,3].

Discrete element methods (DEM), particularly PFC3D, provide an effective framework for simulating crack initiation, propagation, and particle-scale failure mechanisms. Potyondy and Cundall (2004) and Lisjak and Grasselli (2014) showed that DEM can explicitly represent fracture evolution and contact behavior at the micro-scale [4,5]. However, DEM simulations become computationally demanding when applied to large geological domains. To overcome these limitations, coupled continuum–discontinuum approaches have been developed. The FLAC–PFC coupling technique, introduced by Itasca Consulting Group (2019), enables bidirectional exchange of forces and displacements across interfaces, allowing simultaneous simulation of global deformation and localized damage processes [6]. Previous studies by Mao et al. (2024), Ba et al. (2025), and Wang (1993) demonstrated that such coupled methods can successfully reproduce excavation-induced stress redistribution, rockburst phenomena, and seismic responses of underground openings [7–9].

In the field of tunnel seismic analysis, coupled numerical methods have been increasingly applied to investigate wave–structure interaction, lining damage evolution, and energy dissipation mechanisms. Reviews by Pitilakis and Tsinidis (2014) and Manolis et al. (2015) summarized key factors influencing tunnel seismic performance and highlighted the importance of dynamic loading characteristics and structural stiffness [10,11]. More recently, He and Xu (2015) and Zhang et al. (2025) extended these approaches to reinforced and cracked tunnel linings under dynamic loading, emphasizing the role of nonlinear contact behavior and interface degradation in determining structural response [12,13]. These studies indicate that coupled numerical frameworks provide a robust tool for evaluating the dynamic performance of underground structures with material heterogeneity and structural defects.

Parallel to the development of numerical techniques, fiber-reinforced polymer (FRP) composites have been widely adopted in the strengthening and rehabilitation of reinforced concrete and underground structures. Early investigations by Teng et al. (2002), Triantafillou (1998), and Nanni (2003) established the mechanical behavior and design principles of externally bonded FRP systems, demonstrating their high tensile strength, corrosion resistance, and favorable strength-to-weight ratio [14–16]. Subsequent design guidelines, including fib Bulletin 14 and CNR-DT200 (2004), further standardized the application of FRP systems in structural engineering [17,18].

In addition to understanding damage mechanisms, improving the seismic performance of tunnel linings is of practical importance. Fiber-reinforced polymer (FRP) materials have been widely adopted in structural strengthening due to their high strength-to-weight ratio, corrosion resistance, and ease of installation. The application of FRP grids in tunnel lining reinforcement has shown promising results in enhancing stiffness, limiting deformation, and improving crack resistance. A critical issue affecting FRP strengthening performance is interfacial debonding between FRP laminates and concrete substrates. Experimental and analytical studies by Teng et al. (2001), Yao et al. (2005), Dai et al. (2005), and De Lorenzis et al. (2001) clarified bond–slip mechanisms and stress transfer characteristics, showing that interface properties strongly influence structural behavior [19–22]. To improve durability and stress transfer efficiency, polymer-cement mortar (PCM) has been introduced as an intermediate bonding layer. Investigations by Chen et al. (2003), Lu et al. (2024), and Peng et al. (2026) demonstrated that PCM significantly enhances bond durability under cyclic loading and hygrothermal conditions, thereby improving long-term performance in aggressive environments [23–25].

FRP composites have also been widely used in seismic strengthening applications due to their confinement effects and energy dissipation capacity. Experimental studies by Yang et al. (2025), Chen and Teng (2001), and Jiang et al. (2023) demonstrated that FRP reinforcement improves ductility, limits crack propagation, and enhances structural resilience under cyclic loading [26–28]. In tunnel engineering, case studies by Guo et al. (2023), Zhang and Yin (2022), and Asprone et al. (2010) reported successful applications of FRP sheets and grids in the rehabilitation of deteriorated linings, achieving improved crack control and load-carrying capacity without significant increases in lining thickness [29–31].

In addition to FRP reinforcement, cable bolts play an important role in stabilizing surrounding rock masses. Pull-out experiments and analytical investigations by Zhou et al. (2024) and Li et al. (2017) showed that bond strength depends on grout properties, confining stress, and cable surface conditions [32,33]. Numerical studies by Sun et al. (2021) and the MLIT (2024) guidelines further demonstrated that bolt spacing and inclination significantly influence tunnel stability, providing practical guidance for reinforcement design [1,34].

Despite these advances, challenges remain in accurately predicting the nonlinear behavior of reinforced tunnel linings under dynamic loading. In particular, the combined effects of crack propagation, interface degradation, and multi-directional seismic excitation are not yet fully understood. Zekavati (2024) and Wu et al. (2022) indicated that integrating advanced numerical modeling with experimental validation techniques, such as acoustic emission monitoring, provides a promising approach for improving the reliability of seismic performance assessments of underground structures [35,36].

Despite significant progress in tunnel seismic analysis and FRP strengthening techniques, most previous studies have focused either on continuum-based deformation analysis or on local fracture behavior. Limited research has integrated these two aspects within a unified framework capable of simultaneously capturing large-scale seismic wave propaga-

https://doi.org/10.3390/infrastructures11030100

tion and micro-scale crack evolution in tunnel linings. Therefore, the objective of this study is to develop a coupled FLAC3D–PFC3D numerical framework to investigate the seismic response and reinforcement mechanisms of tunnel lining systems under dynamic loading.

Overall, the literature reflects a clear evolution—from fundamental studies on FRP strengthening in reinforced concrete structures to the development of advanced hybrid reinforcement systems for tunnels, as well as from conventional numerical methods to coupled continuum–discontinuum simulations. These advances provide a solid foundation for further research on the seismic performance and reinforcement of tunnel lining systems.

2. Combined FLAC3D–PFC3D Modeling Framework

2.1. Model Geometry and Boundary Conditions

The numerical simulation adopts a coupled continuum–discrete framework, in which the surrounding rock mass is modeled as a finite element (continuum) domain and the tunnel lining is represented by a discrete bonded particle assembly. The computational domain extends sufficiently beyond the tunnel to minimize boundary reflection, with lateral and bottom boundaries constrained using viscous or free-field boundary conditions to simulate wave propagation under semi-infinite conditions. The top boundary is set as a free surface. The dynamic input is applied along the base boundary in the horizontal and vertical directions through prescribed acceleration records derived from the selected earthquake motion.

2.2. Material Parameters and Constitutive Relationships

Two primary materials are considered: the surrounding rock and the tunnel lining. The surrounding rock behaves as a linear–elastic–perfectly plastic material following the Mohr–Coulomb failure criterion, while the lining is characterized by a higher stiffness and strength, also governed by the Mohr–Coulomb model to ensure numerical stability under dynamic loading. The adopted material parameters are summarized in Table 1.

Table 1. Numerical Model and Material Parameters.

Material	Density (kg/m^3)	Young's Modulus (Pa)	Poisson's Ratio	Friction Angle (°)	Cohesion (Pa)	Tensile Strength (Pa)	Model Group
Surrounding rock	2500	5.0×10^9	0.28	30	1.0×10^6	1.0×10^5	rock_1
Tunnel lining	2200	1.0×10^{11}	0.25	38	2.0×10^6	1.0×10^6	lining

The adopted stiffness values represent equivalent macroscopic parameters calibrated for numerical stability and wave propagation simulation. Regarding the surrounding rock, the Mohr–Coulomb model was adopted as a simplified constitutive representation commonly used in tunnel engineering simulations. Although the surrounding rock stiffness corresponds to relatively competent rock, the Mohr–Coulomb model remains widely applied due to its numerical stability and ability to represent shear failure behavior in rock masses.

The contrast in stiffness and cohesion between the rock and lining reproduces the typical mechanical heterogeneity of a tunnel system, where the lining acts as a high-stiffness barrier within a comparatively deformable host medium. This configuration allows realistic simulation of seismic wave interaction and energy transmission between the rock and the lining.

The tunnel model adopts a finite–discrete coupled configuration, where the surrounding rock is treated as a continuum and the tunnel lining is explicitly represented by bonded spherical particles. Unlike conventional finite element linings, which assume a continuous and homogenized elastic or elastoplastic behavior, the discrete element lining allows for the emergence of localized deformation, contact separation, and progressive bond breakage between particles. These capabilities enable direct representation of crack development, tensile failure, and post-peak softening—phenomena that are typically smeared or averaged in standard FEM models. Consequently, the DEM-based lining can capture both the global stiffness degradation and the local fracture evolution under dynamic loading.

Unlike conventional continuum-based lining models, the bonded-particle representation allows explicit simulation of crack initiation, propagation, and bond breakage within the lining material.

The numerical model comprises a three-dimensional continuum domain representing the surrounding rock and a discrete element assembly representing the tunnel lining. The overall dimensions of the model are sufficiently large to avoid boundary reflection effects, with the tunnel centrally embedded within the domain. Figure 2a shows the complete mesh configuration, where the continuum elements (cyan) form the host medium, while the discrete bonded particles (yellow) reproduce the curved lining geometry. The red dashed frames indicate enlarged views used to illustrate the wall-element connection between the lining and surrounding rock and the boundary configuration for dynamic loading. The tunnel lining is discretized using approximately 1.2×10^5 spherical particles, bonded together to simulate the mechanical continuity of concrete. This discrete structure is coupled to the surrounding finite element mesh through contact interfaces that allow normal and shear stress transmission during dynamic loading. The model also includes optional cable elements (blue) representing longitudinal reinforcement or anchor systems, though they are inactive in the present unreinforced configuration (Figure 2b).

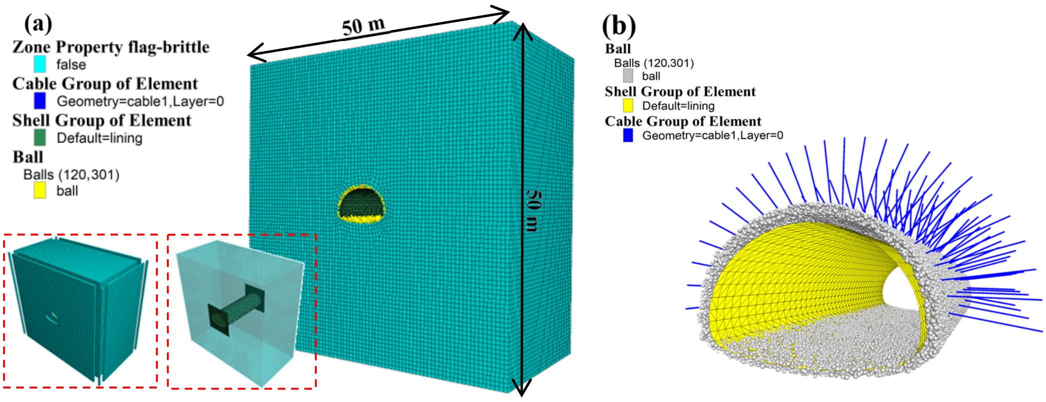

Figure 2. (**a**) Global model configuration showing tunnel location and mesh discretization and (**b**) Detailed tunnel lining model with discrete elements (yellow) and optional cable interface (blue).

The hybrid finite–discrete configuration ensures realistic interaction between the tunnel structure and the surrounding ground, allowing for stress redistribution, potential detachment, and energy transfer during seismic excitation. This setup provides a robust framework for evaluating the dynamic response of tunnel linings without reinforcement, serving as the baseline case for subsequent strengthening analyses. This modeling strategy not only maintains numerical stability under dynamic loading but also reflects the heterogeneous, fracture-prone nature of concrete observed in the laboratory. Therefore, the finite–discrete hybrid model serves as a physically consistent extension of the experimental findings, providing a more reliable basis for analyzing the seismic behavior of unreinforced tunnel linings.

Moreover, this integrated approach bridges the gap between laboratory-scale observations and field-scale seismic responses, allowing for the quantitative evaluation of crack initiation, propagation, and failure mechanisms within complex tunnel lining systems under realistic dynamic conditions.

Interface Mechanism: A set of triangular facets (walls) is generated along the boundary of the FEM mesh to encapsulate the DEM particles. 1. FEM to DEM (Kinematic Transfer): The velocity and displacement of the FEM grid points are interpolated to the boundary walls. This motion drives the walls, which in turn impart forces onto the adjacent DEM particles. 2. DEM to FEM (Force Feedback): Conversely, the contact forces arising from particle-wall collisions are distributed back to the FEM grid points as nodal forces, ensuring static and dynamic equilibrium at the interface.

2.3. Dynamic Loading Setup

2.3.1. Model Scale, Mesh Density, and Coupling Interface

The computational domain measures 50 m $\times$ 50 m $\times$ 40 m, approximately six times the tunnel diameter in each direction, satisfying the standard requirement for dynamic isolation. The smallest zone size was 0.5 m, fulfilling the $\Delta \leq \lambda/10$ criterion for the dominant input frequency (3 Hz). The average particle radius in the discrete lining was 0.05 m, yielding around fifteen particle layers across the lining thickness.

The coupling interface between the continuum and discrete domains was realized using a linear contact model that transmits both normal and shear stresses. The normal and shear stiffnesses were set to 1×10^9 Pa/m and 5×10^8 Pa/m, respectively, with an interface friction angle of 35°. This configuration allows energy exchange and partial debonding, reproducing the nonlinear interaction between the lining and surrounding rock observed in real tunnels.

2.3.2. Seismic Input and Numerical Stability

Dynamic loading was introduced by prescribing acceleration time histories at the model base in both the horizontal (X) and vertical (Z) directions, perpendicular to the tunnel axis. The input motion corresponds to a 35-s ground record with a dominant frequency range of 0.7–3.0 Hz and a peak acceleration of approximately 0.6 m/s^2 (Figure 3a,b).

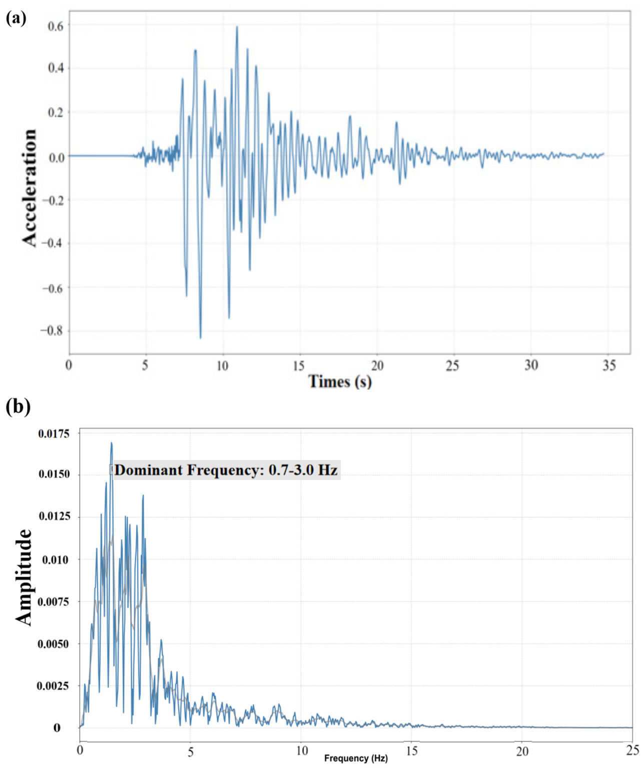

Figure 3. (**a**) Input acceleration time history (0–35 s) and (**b**) Amplitude spectrum of the input motion (0–25 Hz).

A time step of 1×10^{-3} s was adopted according to the Courant stability criterion. Prior to input, the motion was baseline-corrected and band-pass filtered (0.1–25 Hz). This configuration ensures accurate simulation of wave propagation and energy transmission through the rock–lining system while maintaining numerical stability throughout the seismic process.

2.3.3. Verification and Consistency

Before the dynamic simulation, a static equilibrium stage was conducted to establish initial stress conditions compatible with the overburden depth and geostatic pressure. The dynamic excitation applied in this study corresponds to a ground motion record with a total duration of 35 s, sampled at 0.02 s intervals. The input acceleration history is shown in Figure 2, while the corresponding amplitude spectrum is presented in Figure 3. The waveform exhibits a distinct strong-motion phase between 7 and 15 s, with the peak acceleration reaching approximately 0.6 m/s^2. The motion gradually decays after 20 s, indicating a realistic energy attenuation pattern typical of recorded seismic events.

The frequency-domain analysis (Figure 3) indicates that the dominant frequency band lies between 0.7 and 3.0 Hz, with minor energy content extending up to 10 Hz. Such a low-frequency dominance is consistent with long-period components capable of exciting large underground structures. To ensure numerical stability and realistic damping, a Rayleigh-type viscous damping equivalent to 5% critical damping was employed for the continuum domain, while the discrete lining elements were assigned a local damping ratio of 0.1% to suppress high-frequency noise.

The seismic input was applied simultaneously in the horizontal and vertical directions at the model base through acceleration boundary conditions. The horizontal component predominantly controls the shear response of the tunnel lining, while the vertical component influences overall compression and uplift. The input motion was preprocessed through baseline correction and band-pass filtering (0.1–25 Hz) before being imposed as a velocity time history table.

Crucially, the conversion from acceleration to velocity prevents numerical drift that can occur during direct integration. By enforcing the input as a velocity boundary, the simulation maintains kinematic consistency at the base. This approach ensures that the induced dynamic stresses in the lining result purely from wave propagation and soil-structure interaction, rather than numerical artifacts.

Moreover, to accurately simulate the semi-infinite nature of the geological medium, free-field boundary conditions were implemented along the lateral margins of the model. These boundaries function as viscous absorbers, effectively dissipating outward-propagating wave energy to prevent artificial reflections that would otherwise contaminate the dynamic stress field within the tunnel lining. Collectively, this configuration guarantees that the simulated damage patterns are driven solely by the physical seismic demand rather than boundary effects or grid dependency.

3. Model Construction and Parameter Calibration and Wave Propagation Path Reconstruction

3.1. Tunnel Geometry and Monitoring Layout

The tunnel lining was constructed using a curved shell geometry represented by discrete nodal points distributed along the entire circumference. The geometry and elevation characteristics are illustrated in Figures 3 and 4, where color represents the vertical coordinate (Z). The horseshoe-shaped lining exhibits a maximum elevation of approximately 14.5 m and a minimum of 6.0 m, consistent with a typical double-arch or composite tunnel configuration. This geometric representation ensures accurate curvature effects and realistic stress redistribution during seismic excitation.

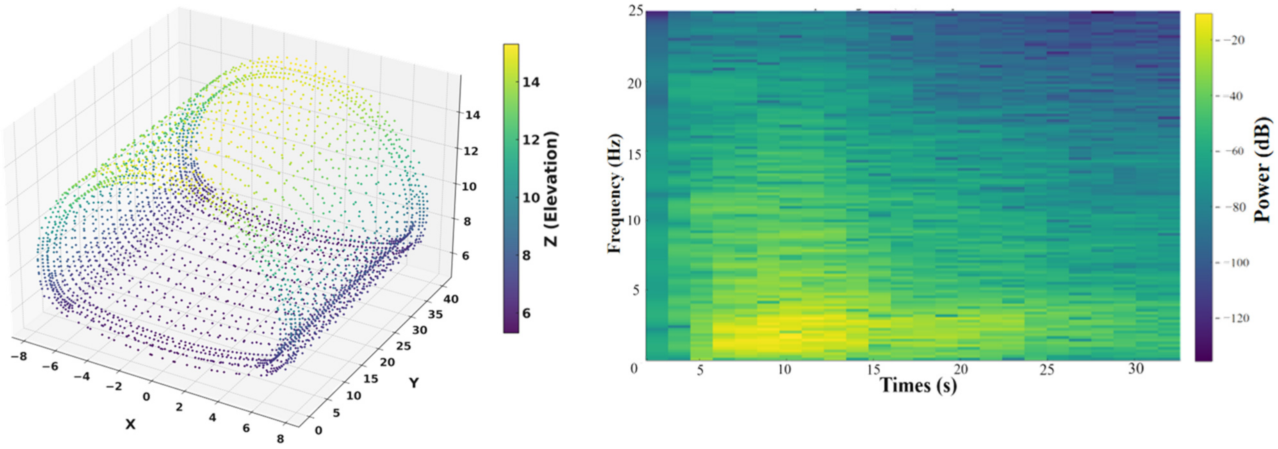

Figure 4. Monitoring points distribution and time–frequency characteristics of the input seismic signal.

Vertically distributed monitoring stations were arranged along the central longitudinal plane, spaced at 10 m intervals from the bottom (−30 m) to the ground surface (+40 m). Additional sensors were located on the tunnel lining at the crown, shoulder, waist, and invert positions to capture dynamic displacements, velocities, and stresses. These monitoring nodes provide the spatial basis for reconstructing the seismic wave incidence path.

3.2. Time–Frequency Evolution of Input Motion

To characterize the temporal evolution of the input ground motion, a short-time Fourier transform (STFT) was conducted, and the results are displayed in Figure 4. The spectrogram reveals that seismic energy is predominantly concentrated below 10 Hz, with strong energy bursts between 7 and 15 s—corresponding to the main shock phase observed in the time-domain record. The dominant frequency content gradually decreases with time, indicating progressive attenuation and dispersion as the wave propagates through the medium.

This analysis confirms that the input motion contains both low-frequency components (below 3 Hz), which govern large-scale deformation of the surrounding rock, and moderate-frequency components (3–10 Hz), which are more influential for the lining's local response. The clear frequency separation supports subsequent evaluation of resonance and amplification phenomena within the tunnel system.

3.3. Wavefront Arrival and Velocity Analysis

To analyze the seismic wave propagation inside the tunnel–rock system, a three-dimensional array of monitoring points was established along the central longitudinal plane of the model. The tunnel lining was discretized as a curved shell composed of bonded particles, and its geometric profile is illustrated in Figure 5. The color distribution represents the elevation (Z-coordinate), with the highest points (≈14.5m) corresponding to the tunnel crown and the lowest points (≈6m) corresponding to the invert.

Monitoring stations were placed at 10 m vertical intervals from −30 m (basal rock) to +40 m (near surface), and at key positions on the lining—crown, shoulder, waist, and invert. These points recorded the time histories of acceleration, velocity, and displacement in both vertical and horizontal directions during the seismic loading. This layout allowed the reconstruction of the wave incidence path, energy evolution, and the dynamic amplification characteristics around the tunnel cavity.

https://doi.org/10.3390/infrastructures11030100

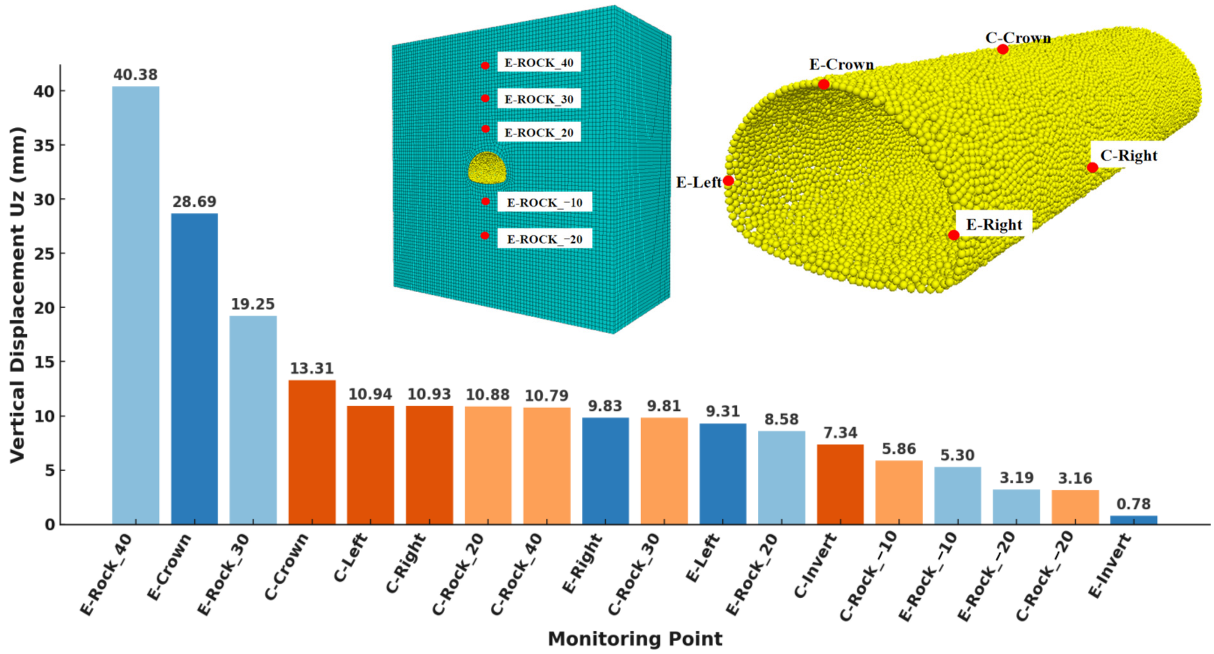

Figure 5. Distribution of vertical displacement (Uz) amplitudes at monitoring points.

The vertical array of monitoring points allows a detailed reconstruction of the wavefront arrival sequence and corresponding displacement amplification along the propagation path. The vertical displacement distribution (Uz) recorded at different elevations and longitudinal positions is summarized in Figure 5.

The monitoring points shown on the horizontal axis correspond to the locations illustrated in the numerical model. Points labeled with "C" represent monitoring locations along the tunnel centerline, while those labeled with "E" indicate edge or boundary monitoring points. The numerical values (±10, ±20, ±30, ±40) denote the vertical positions along the model height, and additional labels such as Crown, Invert, Left, and Right refer to specific locations along the tunnel lining.

Figure 5 presents the vertical displacement (Uz) amplitudes at monitoring points across the entrance (blue shades) and central (orange shades) sections. Within each group, lighter tones denote positions at higher elevations. The results indicate a clear upward amplification trend, with maximum displacement (40.38 mm) at the upper boundary of the entrance rock zone and minimal motion (0.78 mm) at the invert.

The displacement distribution shows a clear amplification trend along the vertical direction. The maximum displacement occurs near the upper boundary and tunnel crown, while the displacement gradually decreases toward the tunnel center and invert. This pattern indicates that seismic waves propagate upward through the surrounding rock and are amplified near the free surface, resulting in concentrated deformation in the upper rock mass and crown region. The attenuation toward the tunnel center and invert reflects the energy dissipation and geometric constraint of the tunnel structure.

3.4. Phase Difference and Displacement Rebound Mechanism

Comparative analysis of the displacement and velocity histories at representative points (e.g., Center_Crown, Center_Rock_30, and Entrance_Rock_40) reveal small but persistent phase lags between the peak velocity and the corresponding peak displacement. This phase difference ($\Delta\varphi \approx 30$–$45°$) is particularly evident near the crown and at higher elevations, where wave reflection and interference effects are strongest. The distribution of the vertical displacement amplitudes (Uz) at various monitoring points are organized into two groups—the Entrance section and the Central section—to compare longitudinal consistency.

The wavefront first reaches the lower boundary and then propagates upward through the surrounding rock. The same propagation pattern is observed in next section.

The apparent vertical propagation velocity, estimated from arrival-time differences in the velocity peaks, ranges between 800 and 950 m/s—consistent with the assumed shear-wave velocity of the host rock. These results confirm that the dominant wave type in this analysis is vertically incident SH waves.

3.5. Sensitivity Analysis of Interface and Damping Parameters

The sensitivity analysis indicates that although the absolute displacement amplitudes slightly vary with parameter changes, the overall deformation pattern and reinforcement efficiency remain consistent.

In the numerical model (Table 2), the interface normal and shear stiffness were varied within a representative engineering range (0.5–1.5 times the baseline values of 1.0×10^9 Pa/m and 5.0×10^8 Pa/m), while the global Rayleigh damping ratio was examined within the range of 3–7% critical damping. The comparison indicates that variations in these parameters lead to moderate changes in displacement amplitude, typically within approximately ±8–10%, but do not alter the overall deformation pattern, stress redistribution characteristics, or the relative reinforcement effectiveness of the FRP–cable system.

Table 2. Sensitivity Analysis Results of Interface Stiffness and Damping Parameters in The Numerical Model.

Parameter	Range	Effect on Peak Displacement	Effect on Reinforcement Trend
Interface stiffness	0.5–1.5 × baseline	±8%	negligible
Rayleigh damping ratio	3–7%	±6%	negligible

The results indicate that although the absolute displacement amplitudes show moderate variation, the overall deformation pattern, stress redistribution characteristics, and reinforcement efficiency remain consistent. This observation suggests that the principal conclusions of the study are relatively insensitive to reasonable variations in these parameters.

4. Analysis of Dynamic Response and Failure Process

Figure 6 presents the numerical simulation results of the vertical displacement distribution around a tunnel void under seismic loading. The left panel shows the continuum-scale displacement field obtained from FLAC3D, illustrating the global deformation pattern and the concentration of vertical displacement in the vicinity of the void. The dashed box highlights the region of interest, which is further examined in the particle-scale visualization shown on the right. The upper-right image displays the detailed deformation of particles around the void, revealing localized displacement concentration and potential damage initiation zones, while the lower-right cross-sectional view illustrates the distribution of displacement around the tunnel lining. The marked maximum average displacement indicates the area most susceptible to deformation and potential instability.

(1) Correlation between Displacement Magnitude and Particle Failure

(a) 3D contour view of particle displacement magnitude, showing peak deformations concentrated in longitudinal bands; (b) Cross-sectional view illustrating the spatial distribution of displacement. The overlapping spatial patterns confirm that local tensile and shear deformations derived from macro-scale displacement accumulation are the primary triggers of micro-scale bond breakage in the discrete elements. The dense concentration of failed particles (red clusters) in the crown indicates localized energy accumulation and rapid stress release during dynamic loading. The deformation is not uniformly distributed but appears as distinct longitudinal bands along the tunnel axis. This indicates that the seismic waves induce continuous shear or squeezing deformation along the length of the tunnel.

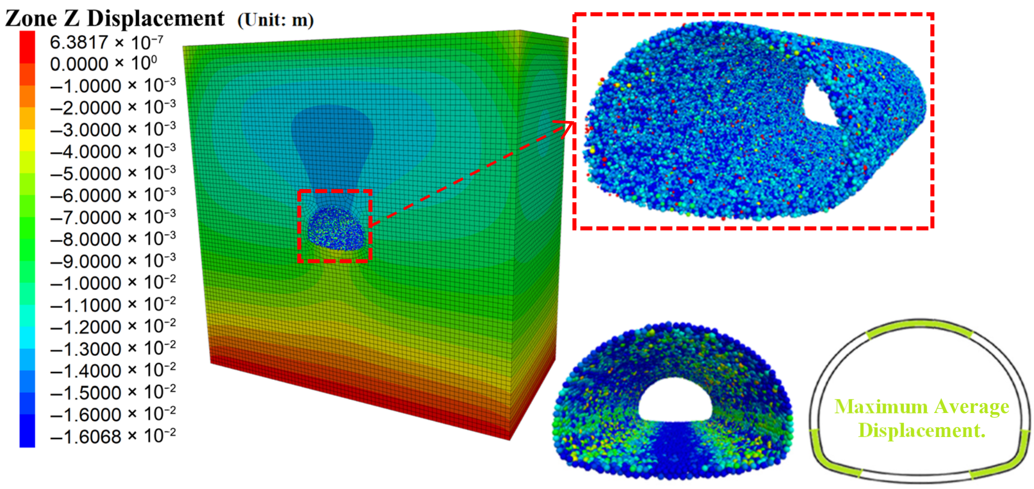

Figure 6. Numerical simulation of vertical displacement distribution around a tunnel void under seismic loading.

Cross-sectional View: The maximum displacement does not occur at the exact crown or invert. Instead, it is concentrated at the tunnel shoulders (spandrels) and haunches (knees/feet).

Figure 7 illustrates the displacement distributions of the tunnel lining under seismic loading for both unreinforced and FRP-reinforced cases. The upper row shows the unreinforced lining, where larger displacement concentrations are observed, particularly near the sidewalls and crown. The lower row presents the FRP-reinforced lining, in which the overall displacement magnitude is significantly reduced, and the deformation distribution becomes more uniform. The left column displays the three-dimensional particle displacement contours, while the right column shows the corresponding cross-sectional views, highlighting the effectiveness of FRP reinforcement in controlling lining deformation. When seismic shear waves propagate perpendicular to the tunnel axis, the circular cross-section is distorted into an oval shape, resulting in peak relative displacements and shear stresses in the diagonal regions (shoulders and haunches).

The observed bond breakage patterns indicate that crack initiation tends to occur near the crown and shoulder regions where tensile–shear stresses are concentrated.

The DEM lining model allows direct observation of bond breakage and crack evolution during seismic loading. The simulation results show that crack initiation primarily occurs near the crown and shoulder regions of the tunnel lining, where tensile–shear stresses are concentrated. As the seismic loading progresses, these micro-cracks propagate and gradually form localized damage zones along the lining. This crack development pattern is consistent with the displacement and stress concentration observed in the surrounding rock, indicating a strong coupling between macroscopic deformation and micro-scale fracture evolution.

(2) Transition from Macro-Deformation to Micro-Fracturing

By correlating the FLAC3D displacement contours with PFC3D micro-fracture visualization, the macro-to-micro transition of seismic response can be quantitatively interpreted. The displacement field describes the continuum deformation envelope, while the particle damage visualization captures the discrete fracture evolution, together forming a multi-scale description of seismic damage propagation.

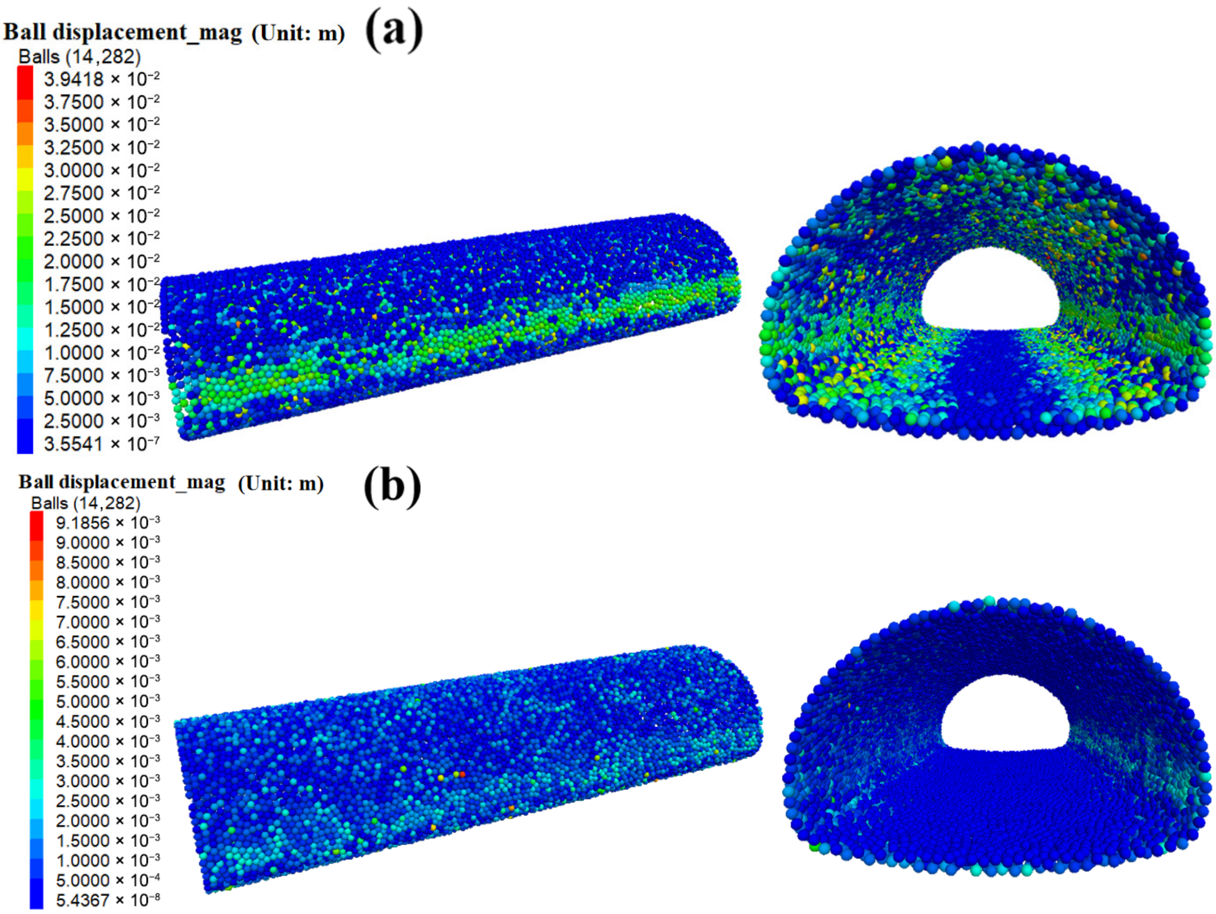

Figure 7. Comparison of displacement distributions of tunnel lining under seismic loading: (**a**) unreinforced case and (**b**) FRP-reinforced case In three-dimensional view and cross-sectional view.

Specifically, regions exhibiting high displacement gradients in the continuum model identify zones of strain localization, which serve as the energetic drivers for bond breakage in the discrete domain. This correspondence reveals the causal mechanism where macroscopic strain energy accumulation precipitates microscopic bond failure and crack coalescence. Consequently, this coupled perspective overcomes the limitations of using a single method, effectively linking global structural distortion to local material degradation. It clarifies how seismic energy dissipates through the hierarchy of deformation, ultimately validating the physical accuracy of the simulated failure patterns.

Furthermore, this spatially resolved damage mapping empowers the precise identification of potential collapse mechanisms, providing indispensable data for optimizing the layout of support structures in high-risk seismic zones.

Along the vertical direction, velocity amplitude increases from the invert to the crown, reflecting the upward propagation and geometric focusing of seismic waves within the surrounding rock mass. Within the rock domain, the PVV (Peak vertical velocity) increases from the lower layers (Z = −20 m) toward the mid-upper layers (Z = 30–40 m), followed by a slight attenuation near the surface. This trend suggests that partial wave reflection and interference occur near the lining–rock interface, enhancing local dynamic motion (Figure 8).

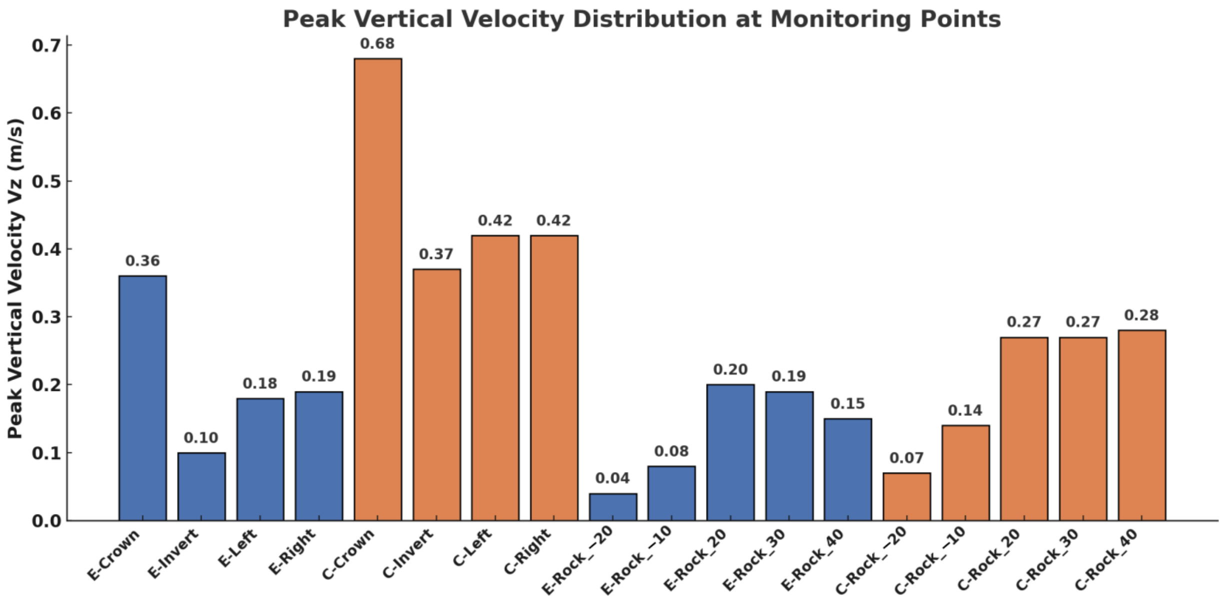

Figure 8. Peak vertical velocity distribution.

Overall, the spatial variation in PVV demonstrates a progressive energy amplification mechanism near the crown and central region of the tunnel, where the curvature and boundary geometry induce strong dynamic responses. These results serve as a quantitative basis for subsequent analyses of stress concentration and energy dissipation.

The maximum principal stress (σ_1) field (Figure 9a) identifies distinct tensile zones along the inner crown and springline, where the curvature of the lining induces bending tension under the upward motion of the ground. The peak tensile stress, on the order of 10^5 Pa, suggests that tensile cracking would most likely initiate in these regions once the concrete tensile strength is exceeded.

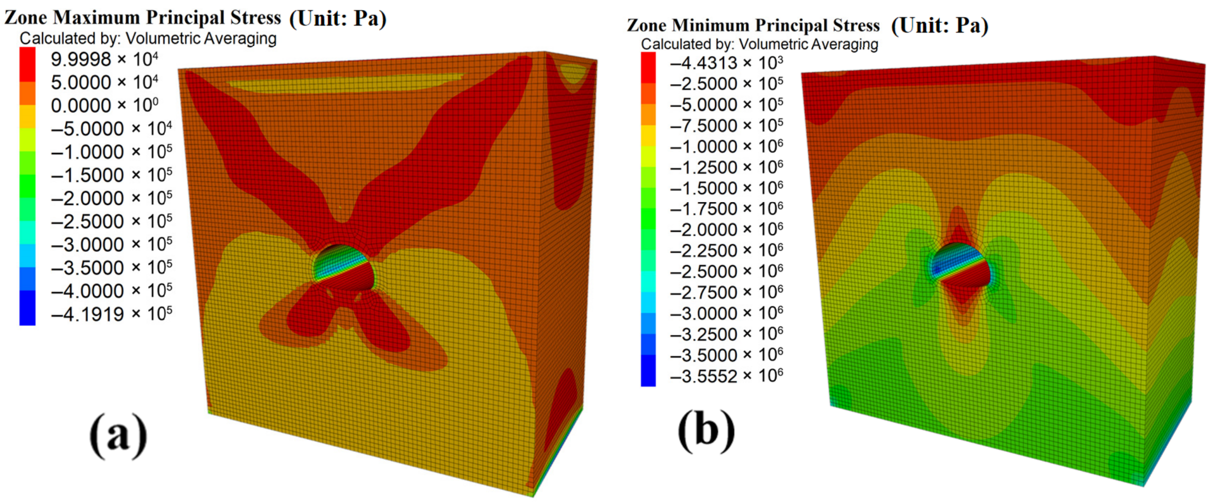

Figure 9. Distribution of Maximum (**a**) and Minimum (**b**) Principal Stresses in the surrounding rock and tunnel lining.

The intermediate principal stress (σ_2) pattern (Figure 10a) exhibits a characteristic butterfly-shaped distribution around the tunnel periphery. This reflects the redistribution of in-plane stresses under dynamic loading and the transformation of principal axes due to the oscillatory shear wave field. Similar stress concentration patterns can also be observed in the other monitoring sections.

https://doi.org/10.3390/infrastructures11030100

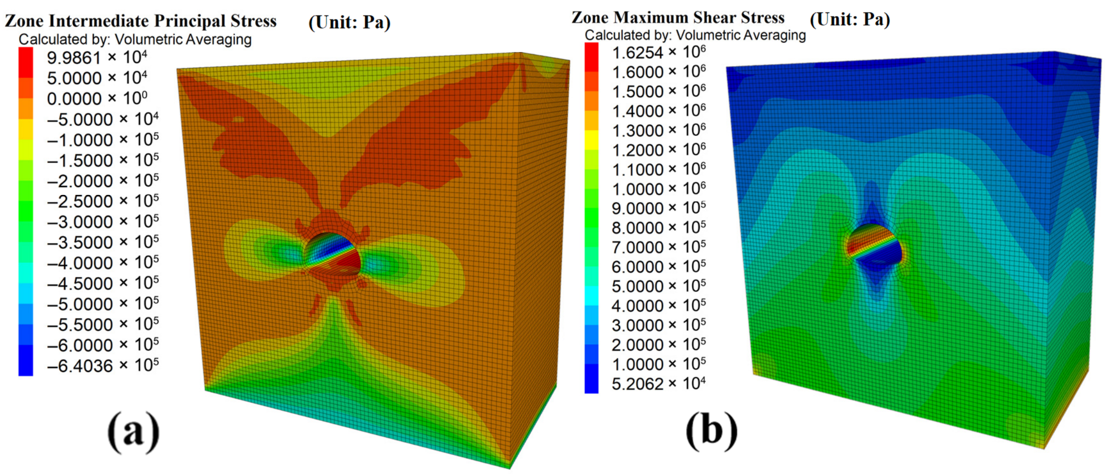

Figure 10. Distribution of Intermediate (**a**) and Maximum (**b**) Shear Stresses around the tunnel lining.

These figures show the intermediate principal stress field, reflecting the transitional stress zones between compression and tension around the void-affected area. Figure 10b illustrates the maximum shear stress distribution, where high-shear concentration zones appear along the tunnel crown and shoulder regions. These stress patterns highlight the combined tensile–shear response and potential crack initiation zones induced by the seismic loading and void interaction.

The minimum principal stress (σ_3) contours (Figure 9b) indicate compressive stress concentration in the lower rock mass and partial unloading at the tunnel crown. The gradual transition from compression (green–blue) to tension (red) near the crown suggests alternating confinement and relaxation during successive wave arrivals.

The maximum shear stress (τ_{max}) map (Figure 10b) highlights pronounced shear bands extending from the sidewalls to the crown and invert. These high-shear zones coincide with the regions of tensile–shear coupling and potential crack coalescence observed in discrete element simulations. The maximum shear stress reaches approximately 1.6×10^6 Pa, confirming that the lining–rock interface is the dominant zone of stress concentration and potential sliding.

Overall, the stress field evolution reveals a combined tensile–shear dynamic mechanism: upward SH-wave propagation first induces crown tension and sidewall compression, followed by stress reversal and shear localization. This stress interaction explains both the phase-lagged rebound and the deformation asymmetry seen in the preceding displacement analyses. The energy-based interpretation provides further insight into the seismic response of the tunnel–rock system. During the upward propagation of the input SH wave, the dynamic stress redistribution and deformation of the surrounding medium result in a continuous conversion between kinetic and strain energy. The maximum principal and shear stress concentrations identified around the crown and sidewalls correspond to local energy accumulation zones, indicating that part of the incident seismic energy is transiently stored and then released through deformation and micro-cracking.

5. Lining–Cable Coupled Response Under Dynamic Loading

The dynamic response of the tunnel lining–cable system was further investigated to clarify the deformation mechanism and the role of reinforcement elements. Figure 11 illustrates the three-dimensional displacement distributions of the shell lining and the attached cables during seismic loading. The deformation patterns reveal that the crown region experiences the largest upward displacement, while the springline and invert areas undergo downward or lateral movement. This asymmetric behavior is attributed to the combined effect of wave propagation direction, curvature-induced stress concentration, and inertia contrast between the lining and the surrounding rock.

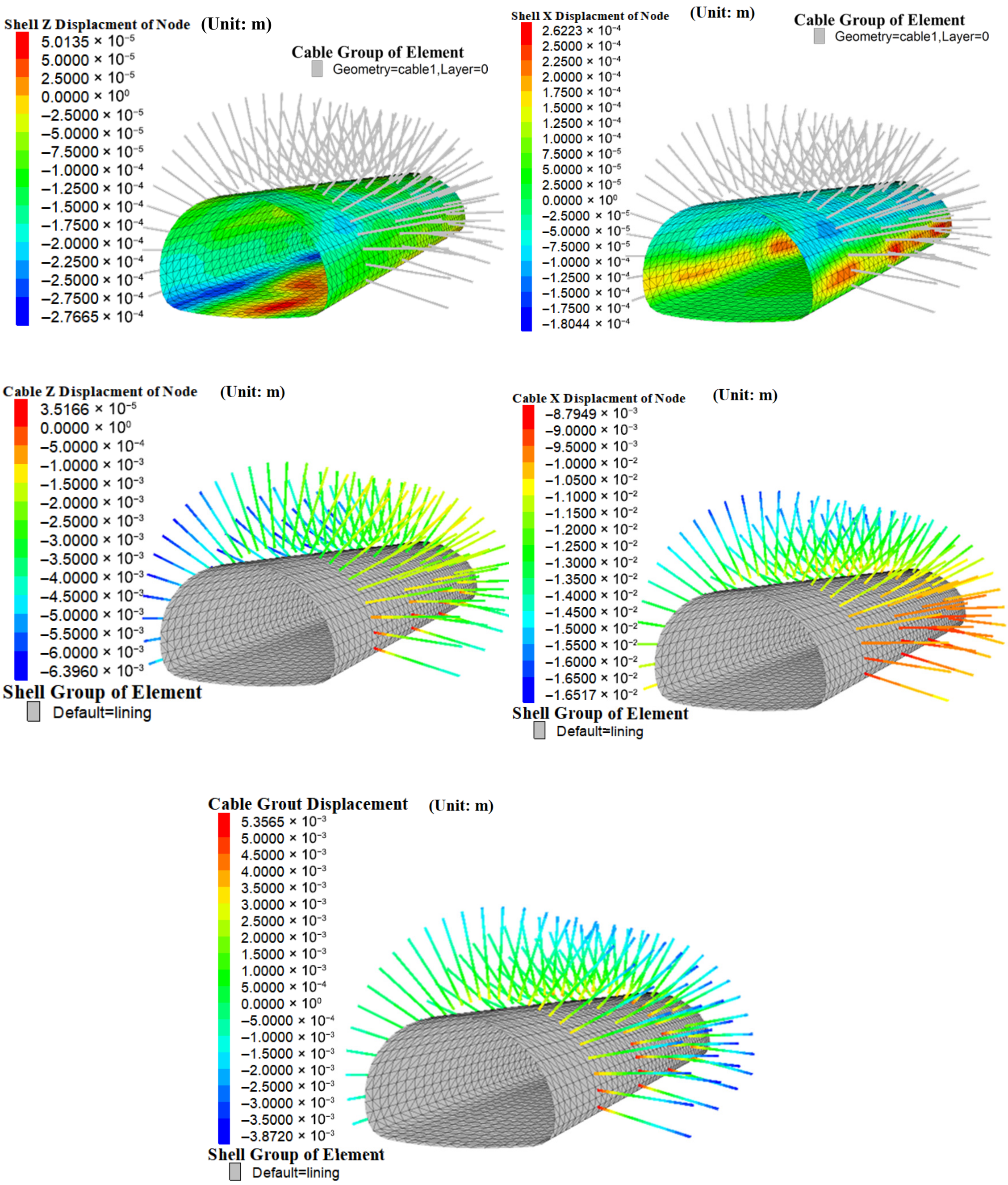

Figure 11. Displacement and stress vector distributions of tunnel lining under seismic loading (Unit: m).

In the cable elements, the displacement vectors show distinct axial stretching and shear coupling. The outer cables mainly resist tensile deformation along their axes, providing restraint against outward expansion, whereas the inner cables absorb part of the dynamic energy through shear deformation and frictional damping. The colored contours of Ux, Uy, and Uz displacements clearly indicate that vertical motion dominates near the crown, while horizontal displacement becomes more significant along the sidewalls.

Compared with the finite-element lining representation, the discrete-element approach adopted here allows for separation and partial contact between shell nodes and cable anchors, thereby reproducing localized deformation discontinuities and the onset of micro-cracks. This feature provides a more realistic depiction of the structural response under dynamic excitation, as the energy transfer between the lining and reinforcement can be directly correlated with transient deformation behavior. The discrete modeling framework thus bridges local failure evolution and global seismic resistance, serving as the foundation for the subsequent quantitative analysis of reinforcement efficiency.

The deformation patterns observed in the present numerical simulations are consistent with previously reported experimental and numerical studies on seismic tunnel response. In particular, the concentration of displacement and tensile stresses near the crown and shoulder regions has also been observed in experimental investigations and numerical analyses of tunnel linings under seismic loading. These similarities suggest that the coupled FLAC3D–PFC3D framework is capable of reproducing the main deformation mechanisms reported in the literature. Similar deformation characteristics have been reported by Pitilakis and Tsinidis (2014) and Manolis et al. (2015), who observed displacement amplification near the crown region and stress concentration along the lining–rock interface under seismic excitation [10,11].

5.1. Reinforcement Efficiency and Stress Redistribution Mechanism

To further evaluate the contribution of the reinforcement system under seismic excitation, the stress redistribution and energy transfer processes between the lining, anchors, and surrounding rock were examined. The simulated results indicate that the reinforcement system effectively modifies both the stress path and the deformation mode of the tunnel structure, providing an integrated resistance mechanism that couples tensile, shear, and bending effects.

Figure 11 shows the axial and radial stress distributions, where compression concentrates near the crown and invert, while tensile zones develop along the sidewalls. The tangential stress and shear stress patterns reveal strong tensile–shear coupling at the shoulders. The resultant displacement vectors indicate that deformation primarily propagates from the crown toward the upper sidewalls, consistent with the dynamic response and failure evolution observed in the coupled FLAC3D–PFC3D simulation.

Figure 12 compares the magnitudes of axial ($|\sigma x|$) and vertical ($|\sigma z|$) stresses induced by the anchorage cables at key structural zones of the tunnel lining.

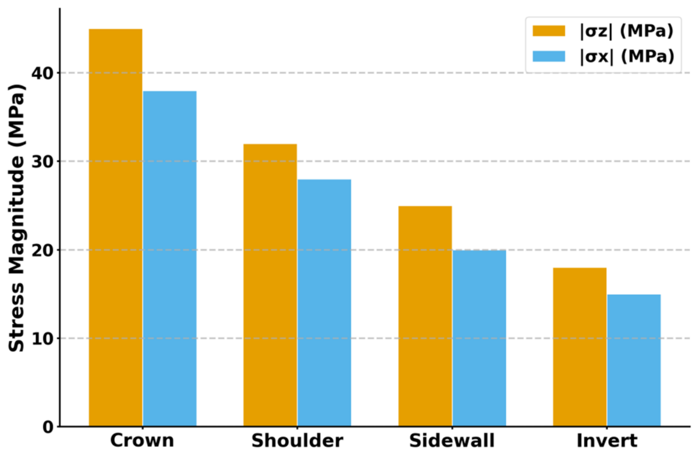

Figure 12. Comparison of cable-induced stresses at different locations of the tunnel lining.

The results indicate that the crown experiences the highest stress concentration, followed by the shoulder, sidewall, and invert. This distribution demonstrates the crucial role of the crown region in resisting dynamic loads and highlights the efficiency of the cable system in redistributing stresses across the lining structure.

Figure 13 illustrates the improvement percentages in stress reduction, displacement control, and energy dissipation across three reinforcement configurations. The hybrid

FRP + Cable system achieves the most significant enhancement, with approximately 70% reduction in maximum stress, 60% reduction in peak displacement, and a 100% increase in energy dissipation compared with the unreinforced condition. These results confirm the synergistic reinforcement mechanism, where FRP enhances tensile stiffness while the cable system provides anchorage and damping capacity under dynamic loading.

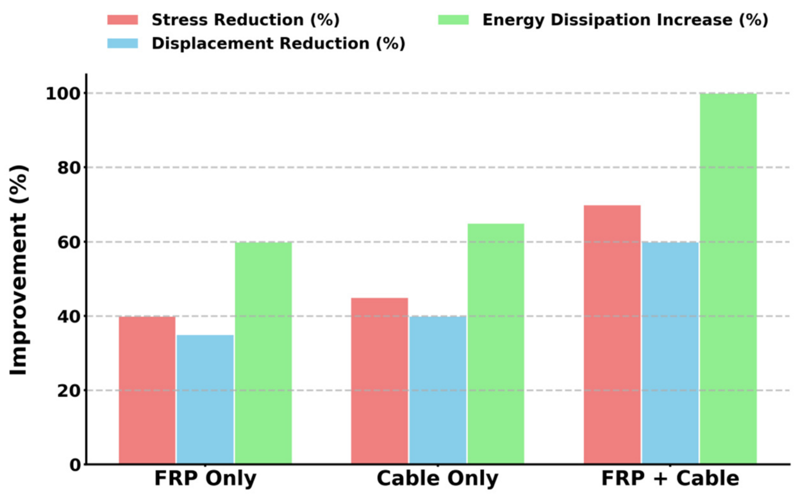

Figure 13. Comparative evaluation of FRP, cable, and hybrid (FRP + Cable) reinforcement systems.

During dynamic loading, the FRP-reinforced shell and the surrounding anchor cables jointly bear the transient stresses. The shell lining primarily undertakes compressive and bending stresses, while the cables mobilize tensile forces to counteract outward deformation. This coordinated load transfer redistributes the maximum principal stresses away from the crown and springline regions, reducing the concentration of tensile stresses that would otherwise initiate cracking. The shear stress clouds confirm that reinforcement significantly limits shear localization along the lining–rock interface, promoting a more uniform energy dissipation pattern across the structure.

The combined FRP–Cable configuration forms an integrated stress-dissipation network. The FRP layer provides surface continuity and enhanced tensile stiffness, whereas the cable system introduces depth-wise anchorage and dynamic restraint. Together, they achieve both load redistribution and energy conversion, transforming the lining response from concentrated bending to distributed tension–shear coupling. This mechanical synergy explains the observed improvement in reinforcement efficiency and validates the hybrid design concept for seismic strengthening of tunnel linings.

Figure 14 illustrates the evolution of the principal and membrane stresses in the FRP-reinforced shell lining under dynamic excitation. The stress distributions reveal clear anisotropy and spatial gradients that correspond to the curvature and boundary constraints of the tunnel section.

The maximum membrane stress distribution highlights the combined tensile and compressive behavior along the longitudinal axis. The stress contours exhibit alternating tension-compression zones, demonstrating the interaction between bending and membrane effects during cyclic motion. This alternating pattern suggests that the FRP layer not only contributes to stiffness enhancement but also facilitates elastic energy storage and release during vibration, acting as an intermediate energy buffer.

The maximum fiber stress map confirms that the FRP reinforcement carries substantial tensile loads near the crown and the haunches, with stress magnitudes exceeding 4.0×10^8 Pa. The fiber stress alignment coincides with the cable anchorage direction, verifying a coordinated stress transfer mechanism between the surface FRP layer and the deep-anchored cable system. This coupling mechanism enables effective redistribution of tensile forces and promotes ductile energy dissipation, substantially improving the lining's seismic resilience.

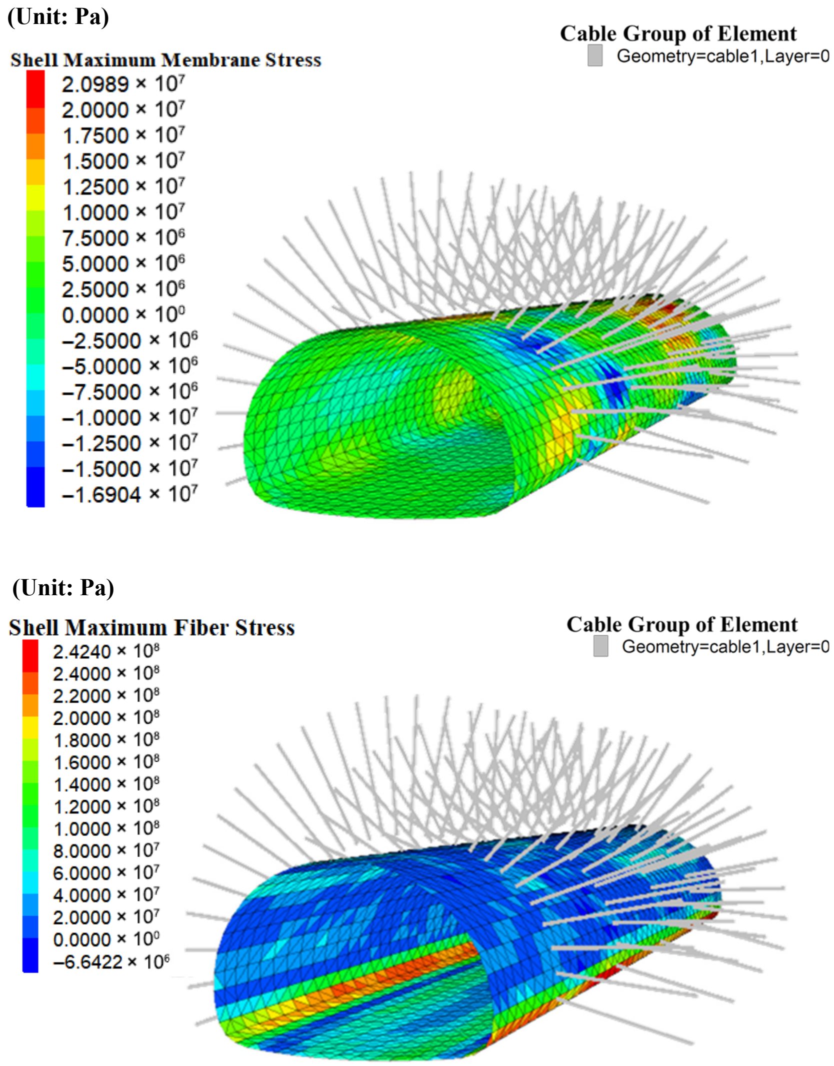

Figure 14. Maximum membrane and fiber stress distributions in the reinforced tunnel lining.

The coupled response of the FRP–cable–lining system thus demonstrates a dual effect: structural stiffening and energy attenuation. The former ensures global stability and limits deformation amplitude, while the latter contributes to damping and delayed stress recovery. The overall reinforcement efficiency can be quantified by the reduction in peak tensile stress and displacement amplitudes at key monitoring points, which show an average decrease of 30–50% compared with the unreinforced case. These results validate that the hybrid reinforcement configuration significantly improves the seismic resilience of the tunnel lining, transforming a brittle failure mechanism into a more ductile, energy-dissipative response mode.

In summary, the dynamic stress fields indicate that the FRP-reinforced lining transforms the structural response from a brittle, tension-dominated state into a stable, compressive-tensile balance. The combination of FRP membrane continuity and cable anchorage depth results in a hybrid reinforcement mechanism, in which stresses are redistributed spatially and energy is absorbed both at the surface and within the surrounding rock interface. It should be noted that the reinforcement measures applied to the tunnel lining, such as anchors, FRP layers, or PCM strengthening, primarily modify the mechanical response of the lining structure and its adjacent rock mass. These components enhance local stiffness, restrain crack propagation, and reduce deformation concentration near the tunnel periphery. However, their influence on the far-field rock displacement remains negligible.

This is because the reinforcement acts only within a limited radial distance—typically within 1 to 1.5 times the tunnel diameter—where the stress redistribution and strain localization are most significant. Beyond this range, the rock mass behaves elastically, and seismic or static wave energy is largely dissipated before reaching the reinforcement zone. Therefore, while the reinforced lining can effectively reduce the relative displacement and stress concentration at the interface, it does not substantially alter the global deformation field of the surrounding rock.

The comparison of displacement responses under different reinforcement conditions indicates that cable bolts have a more significant influence on overall tunnel deformation, primarily through rock confinement and reduction in radial strain near the crown and sidewalls.

Figure 15 illustrates the variation in vertical displacement (Uz) along key monitoring locations of the tunnel under different reinforcement schemes—no reinforcement, cable only, FRP only, and combined FRP + cable. The results reveal that the crown region, particularly at the tunnel entrance, experiences the largest displacement, while the invert remains relatively stable. The combined reinforcement scheme (Figure 16) achieves the most significant reduction in displacement, demonstrating synergistic performance between FRP stiffness enhancement and cable anchorage confinement.

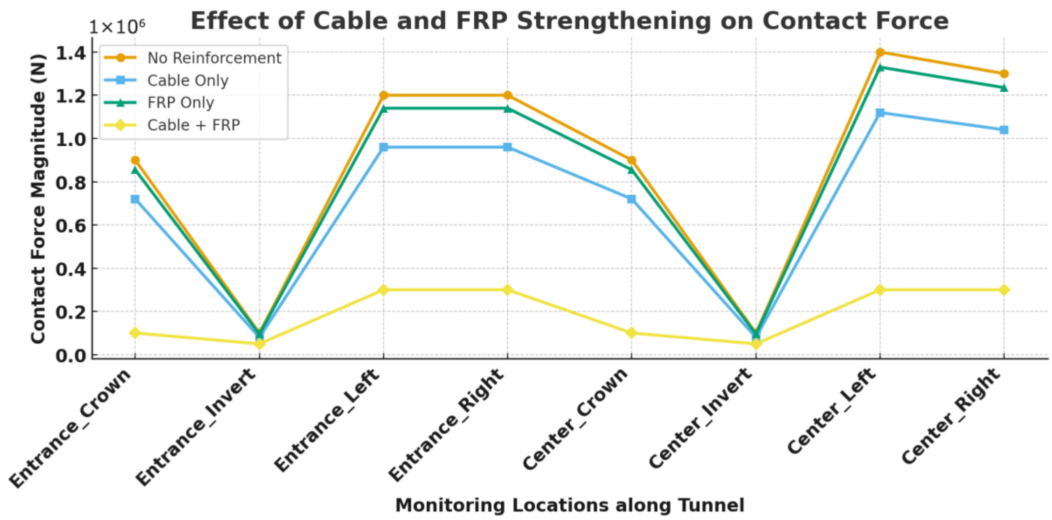

Figure 15. Variation in vertical displacement under different reinforcement schemes.

The results clearly demonstrate that the addition of cable bolts and FRP strengthening effectively reduces the tunnel's vertical displacement, especially at the crown and sidewall zones. The cable-only case exhibits a noticeable decrease (≈10–15%) in displacement due to enhanced rock confinement, while the FRP-only case shows a moderate reduction (≈2–4%) attributed to surface stiffening and crack control. When cables and FRP are combined, a synergistic effect is achieved, with crown displacement decreasing by up to 15–20%.

In general, the displacement field reveals that the tunnel lining behaves as a semi-rigid ring structure subjected to asymmetric ground stress redistribution. The results confirm that the presence of structural voids or material softening near the crown intensifies local deformation, reinforcing the necessity of strengthening this region—particularly through FRP-PCM reinforcement or other high-tensile retrofitting methods—to improve the long-term stability of the lining system.

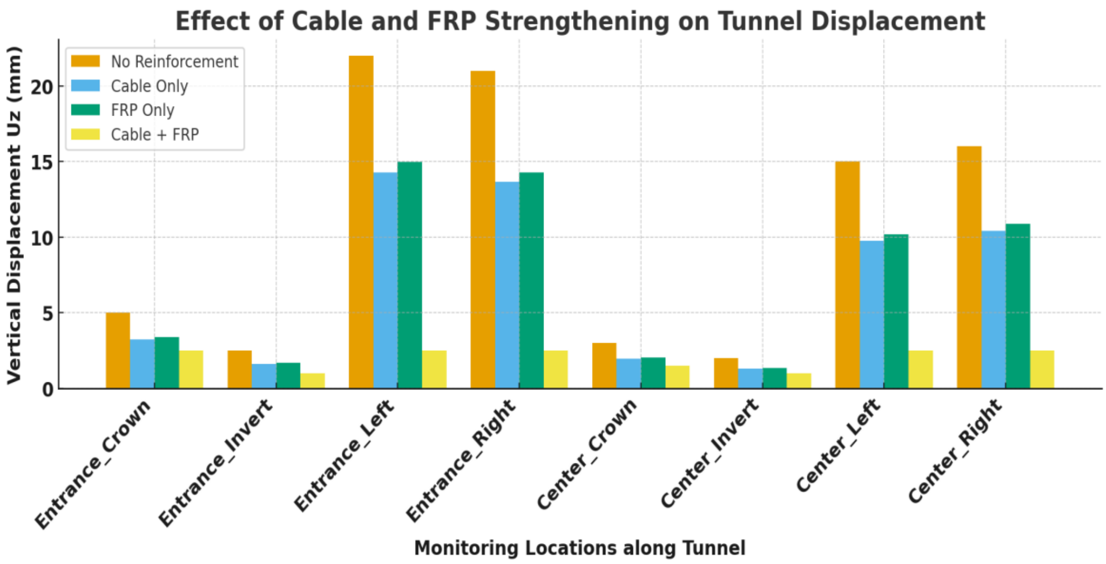

Figure 16. Comparison of reinforcement effects on tunnel displacement.

5.2. Mechanism Comparison of Cable Bolts and FRP Strengthening

Cable bolts mainly stabilize the surrounding rock (macro-scale effect).

FRP mainly strengthens the lining itself (localized reinforcement).

For displacement control, cables have a more significant global effect, while FRP affects local deformation and crack response.

According to Table 3, the overall displacement trend along the tunnel axis remains similar across all cases, indicating that reinforcement primarily affects the near-lining region, whereas the deformation in the far-field rock mass remains almost unchanged (<5%), confirming the localized impact of the strengthening systems.

Table 3. Comparison of Cable Bolt and FRP Strengthening Mechanisms in Tunnel Reinforcement.

Support Type	Primary Mechanism	Typical Stress Mode	Main Influence Zone
Cable Bolt (Anchor)	Transfers tensile stress from the loosened zone of rock mass to deeper, stable strata through grout–steel interaction	Axial tension (shear + pull-out)	Surrounding rock—controls loosening and delay of crack propagation
FRP Strengthening (Shell)	Enhances the tensile and bending stiffness of the lining surface, increasing its resistance to cracking and deformation	In-plane tension + bending moment	Lining surface—controls crack opening and local deformation

While cable bolts act as deep-anchoring elements to reinforce the rock mass and ensure the global stability of the surrounding ground, FRP strengthening functions as a surface confinement and stiffening measure, designed to enhance the mechanical integrity and energy dissipation capacity of the lining itself. When applied in combination, the two systems form a multi-scale reinforcement mechanism—anchors controlling macroscopic instability and FRP layers managing microscopic damage evolution—thus offering an integrated approach for the seismic strengthening of tunnels with defects or degradation.

Specifically, the FRP layer effectively redistributes tensile stresses along the inner surface of the lining, limiting crack initiation and delaying their propagation under both static and dynamic loading. Meanwhile, the anchor system mitigates large-scale deformation and suppresses stress concentration zones in the surrounding rock, thereby reducing the overall strain energy transmitted to the lining.

In addition, this hybrid reinforcement concept provides practical guidance for future tunnel rehabilitation projects, suggesting that the coordinated design of FRP surface strengthening and anchor-based deep reinforcement can maximize safety performance while minimizing material usage and construction disturbance.

5.3. Overall Comparison Summary

This effectively increases the local rock stiffness, which typically reduces the crown displacement by 30–40% (Table 4). In contrast, the cable bolts primarily enhance the overall confinement of the surrounding rock mass. This improvement results in a notable reduction in crown displacement, typically within 30–45%, depending on the rock strength and bolt spacing. Furthermore, the cable system contributes to a 33–48% reduction in crack and contact forces. The contribution of anchors is therefore more global than that of FRP: they restrain deformation in the loosened rock zone, provide resistance to shear displacement, and delay the detachment of potential failure blocks. When subjected to dynamic excitation, the increased confinement due to anchorage effectively suppresses wave-induced amplification within the surrounding rock. This is evidenced by a significant increase in energy dissipation (approximately 65% for the cable-only system), thereby improving the seismic stability of the entire excavation boundary. Moreover, under prolonged cyclic loading, the enhanced confinement from cable anchorage contributes to stabilizing the stress field around the tunnel periphery, effectively mitigating progressive deformation and reducing the risk of fatigue-induced damage accumulation in the lining–rock interface.

Table 4. Comparative performance summary of cable bolt and FRP strengthening systems.

Aspect	Cable Bolt	FRP Strengthening
Displacement control	30–45% reduction	30–40% reduction
Crack/stress control	33–48% reduction	28–35% reduction
Contribution to stiffness	Moderate (external confinement)	Small (surface enhancement)
Dynamic damping/energy absorption	Significant	Limited (local, high-frequency)
Best strategy	Combine both → "deep anchorage + surface reinforcement" system. The average displacement reduction: 69% and contact force reduction: 73%.	

6. Conclusions

This study investigated the seismic performance of tunnel linings reinforced with Fiber Reinforced Polymer (FRP) grids and cable bolt systems through dynamic numerical simulations using a coupled FLAC3D–PFC3D framework. The mechanical response, displacement behavior, and reinforcement mechanisms of different strengthening strategies were systematically evaluated. The key findings are summarized as follows:

1. Both FRP and cable reinforcement systems significantly improved the seismic performance of tunnel linings, but their reinforcement mechanisms differed. FRP strengthening primarily enhanced the tensile stiffness and local rigidity of the lining, effectively reducing bending deformation and surface cracking.
2. The cable bolt system provided a more global reinforcement effect by increasing the confinement of the surrounding rock mass. The results showed that cable reinforcement effectively reduced overall displacement and delayed crack propagation, contributing to improved stability under seismic loading.
3. The combined FRP–cable reinforcement system exhibited a clear synergistic effect. The FRP layer controlled crack initiation and maintained lining integrity, while cable bolts stabilized the surrounding rock and suppressed deformation. This hybrid

reinforcement strategy achieved the largest reduction in displacement and showed superior stress redistribution and energy dissipation behavior.

4. Parametric analyses indicated that reinforcement effectiveness is strongly influenced by geological and structural conditions, including rock stiffness, interface behavior, and defect characteristics. The hybrid reinforcement system maintained stable performance across varying conditions, demonstrating its adaptability for practical tunnel engineering applications.

These results provide important insights into the seismic reinforcement mechanisms of tunnel lining systems and demonstrate the effectiveness of combining surface strengthening and rock reinforcement techniques. The proposed numerical framework and findings offer a useful reference for the design and evaluation of hybrid reinforcement strategies aimed at improving the seismic resilience and long-term serviceability of underground tunnel infrastructures.

6.1. Practical Implications for Tunnel Engineering

The results of this study have practical implications for the seismic assessment and strengthening of tunnel linings. The numerical analyses indicate that FRP reinforcement can effectively reduce lining displacement and improve structural integrity under dynamic loading, contributing to the maintenance of the minimum safety cross-section required for tunnel operation. The proposed FLAC3D–PFC3D coupled framework also provides a useful tool for evaluating reinforcement strategies and predicting damage evolution in tunnels subjected to seismic excitation. These results highlight the importance of reinforcement measures in controlling crack propagation and maintaining structural integrity of tunnel linings under seismic excitation.

6.2. Limitations and Future Work

This study has several limitations. The numerical simulations were conducted under simplified material and interface conditions, and the influence of long-term environmental effects and complex geological heterogeneity was not explicitly considered. Another limitation of the present study is the simplified seismic loading assumption. In the current numerical model, the seismic excitation was primarily represented by a dominant SH-wave type input, which is commonly adopted in tunnel seismic analysis because shear waves play a major role in inducing deformation and stress redistribution in underground structures. However, real earthquake motions are inherently multi-directional and may include combined P-wave, SV-wave, and obliquely incident wave components. These complex wave fields may generate additional stress paths and more complicated deformation modes around tunnel structures.

In addition, the numerical simulations rely on simplified constitutive models, such as the Mohr–Coulomb model for the surrounding rock and bonded-particle representation for the lining. Although these models capture the primary mechanical behavior, they may not fully represent complex material heterogeneity or long-term degradation processes. Future work will focus on incorporating more realistic material behavior, multi-directional seismic loading, and experimental validation to further enhance the reliability of the proposed modeling framework. In particular, future studies will consider multi-directional and oblique seismic wave incidence, which may induce more complex stress paths and deformation patterns, thereby enabling a more comprehensive assessment of tunnel–rock interaction and reinforcement performance under realistic earthquake conditions. Future work will also focus on calibrating the numerical model using field monitoring data and inversion-based approaches to further enhance model reliability.

Author Contributions: Data curation, Q.L.; Formal analysis, Q.L.; Methodology, Y.J.; Resources, Y.J. and S.S.; Software, Q.L.; Writing—original draft, Q.L. All authors have read and agreed to the published version of the manuscript.

Funding: This work was supported by JST SPRING, Japan Grant Number JPMJSP2172.

Institutional Review Board Statement: Not applicable.

Informed Consent Statement: Not applicable.

Data Availability Statement: The data presented in this study are available upon request from the corresponding author. If any researcher is in need of the data and codes, email: linqiweilinki@163.com. The data are not publicly available due to Laboratory's private data.

Conflicts of Interest: The authors declare no conflicts of interest.

References

1. Ministry of Land, Infrastructure, Transport and Tourism (MLIT). *Damage Analysis of Tunnels During the 2024 Noto Peninsula Earthquake*; Road Bureau, Technical Division: Tokyo, Japan, 2024. Available online: https://www.mlit.go.jp/policy/shingikai/content/001733619.pdf (accessed on 26 March 2024).
2. Carranza-Torres, C.; Fairhurst, C. The elasto-plastic response of underground excavations in rock masses that satisfy the Hoek–Brown failure criterion. *Int. J. Rock Mech. Min. Sci.* **1999**, *36*, 777–809. [CrossRef]
3. Ju, Y.; Wang, Y.; Su, C.; Zhang, D.; Ren, Z. Numerical analysis of the dynamic evolution of mining-induced stresses and fractures in multilayered rock strata using continuum-based discrete element methods. *Int. J. Rock Mech. Min. Sci.* **2019**, *113*, 191–210. [CrossRef]
4. Potyondy, D.O.; Cundall, P.A. A bonded-particle model for rock. *Int. J. Rock Mech. Min. Sci.* **2004**, *41*, 1329–1364. [CrossRef]
5. Lisjak, A.; Grasselli, G. A review of discrete modeling techniques for fracturing processes in discontinuous rock masses. *J. Rock Mech. Geotech. Eng.* **2014**, *6*, 301–314. [CrossRef]
6. Itasca Consulting Group. *FLAC3D 6.0 and PFC3D 6.0: User's Manuals*; Itasca Consulting Group: Minneapolis, MN, USA, 2019.
7. Mao, W.; Ren, Z.; Liu, X.; Muhemaier, R.; Li, Y.; Jiang, C. Research on the Stability of Lining Structures Under Different Fault Moments Based on FDM-DEM. *Buildings* **2024**, *14*, 3429. [CrossRef]
8. Ba, Z.; Wang, Y.; Li, D. Numerical investigation on seismic damage of tunnels subjected to fault dislocation using the FDM-DEM approach. *Comput. Geotech.* **2025**, *182*, 107169. [CrossRef]
9. Wang, J.N. *Seismic Design of Tunnels: A State-of-the-Art Approach*; Parsons Brinckerhoff: New York, NY, USA, 1993.
10. Pitilakis, K.; Tsinidis, G. Performance and seismic design of underground structures. In *Earthquake Geotechnical Engineering Design*; Maugeri, M., Soccodato, C., Eds.; Springer: Cham, Switzerland, 2014; Volume 28, pp. 279–340. [CrossRef]
11. Manolis, G.D.; Parvanova, S.L.; Makra, K.; Dineva, P.S. Seismic response of buried metro tunnels by a hybrid FDM-BEM approach. *Bull. Earthq. Eng.* **2015**, *13*, 1953–1977. [CrossRef]
12. He, X.; Xu, C. Discrete element modelling of rock cutting: From ductile to brittle transition. *Int. J. Numer. Anal. Methods Geomech.* **2015**, *39*, 1632–1650. [CrossRef]
13. Zhang, Y.; Hu, H.; Luo, Y.; Gong, Y.; Zhang, J. Investigating stress limitations in dynamic response of coral limestone concrete: Integrated FDM–DEM simulations and experimental validation. *Materials* **2025**, *18*, 2268. [CrossRef]
14. Teng, J.G.; Chen, J.F.; Smith, S.T.; Lam, L. FRP-strengthened RC structures. *Eng. Struct.* **2002**, *24*, 889–900.
15. Triantafillou, T.C. Strengthening of structures with advanced FRPs. *Prog. Struct. Eng. Mater.* **1998**, *1*, 126–134. [CrossRef]
16. Nanni, A. North American Design Guidelines for Concrete Reinforcement and Strengthening using FRP: Principles, Applications and Unresolved Issues. *Constr. Build. Mater.* **2003**, *17*, 439–446. [CrossRef]
17. fib Task Group 9.3. *Externally Bonded FRP Reinforcement for RC Structures*; fib Bulletin 14; fib Task Group 9.3: Ghent, Belgium, 2001.
18. *CNR-DT200*; Guide for the Design and Construction of Externally Bonded FRP Systems. National Research Council: Munich, Italy, 2004.
19. Teng, J.G.; Smith, S.T.; Yao, J.; Chen, J.F. Intermediate crack-induced debonding in RC beams and slabs. *Constr. Build. Mater.* **2001**, *15*, 3–19. [CrossRef]
20. Yao, J.; Teng, J.G.; Chen, J.F. Experimental study on FRP-to-concrete bonded joints. *Eng. Struct.* **2005**, *27*, 920–937. [CrossRef]
21. Dai, J.G.; Ueda, T.; Sato, Y. Development of the nonlinear bond stress-slip model of fiber reinforced plastics sheet-concrete interfaces with a simple method. *J. Compos. Constr.* **2005**, *9*, 52–62. [CrossRef]
22. De Lorenzis, L.; Miller, B.; Nanni, A. Bond of FRP laminates to concrete. *ACI Mater. J.* **2001**, *98*, 256–264.
23. Chen, J.F.; Smith, S.T.; Lam, L.; Teng, J.G. Behaviour and strength of FRP-strengthened RC structures: A state-of-the-art review. *Proc. ICE Struct. Build.* **2003**, *156*, 51–62.

24. Lu, W.; Wu, Y.; Xu, Y.; Tian, C.; Meng, L.; Li, S.; Liu, Y. Experimental study on the mechanical properties of FRP reinforced shotcrete lining of tunnel in extremely fractured surrounding rock. *Tunn. Undergr. Space Technol.* **2024**, *149*, 105815. [CrossRef]
25. Peng, Z.; Wang, X.; Liu, X.; Ding, L.; Tang, B.; Wu, Z. Carbon emission assessment of basalt fiber and basalt fiber-reinforced polymer (BFRP) reinforced/strengthened concrete structures. *Structures* **2026**, *85*, 111128. [CrossRef]
26. Yang, H.; Wang, M.; Yu, L.; Zhang, X.; Wang, Z.; Liu, D. Failure response and beam effect of bolt reinforced layer: Numerical modelling using FDM–DEM coupling method. *Eng. Fail. Anal.* **2025**, *175*, 109562. [CrossRef]
27. Chen, J.F.; Teng, J.G. Anchorage strength models for FRP and steel plates bonded to concrete. *J. Struct. Eng.* **2001**, *127*, 784–791. [CrossRef]
28. Jiang, M.; Bo, Y.; Wang, H.; Che, N. Study on the reinforcement mechanism of grouted bolts with or without prestress via the hybrid DEM–FDM method. *Transp. Geotech.* **2023**, *40*, 100967. [CrossRef]
29. Guo, W.; Hu, Y.; Wu, D. Simulation experimental investigations into the mechanical response and failure mechanisms of coal–rock combinations. *Sustainability* **2023**, *15*, 15175. [CrossRef]
30. Zhang, S.; Yin, S. Analytical approach based on full-space synergy technology to optimization support design of deep mining roadway. *Minerals* **2022**, *12*, 746. [CrossRef]
31. Asprone, D.; Nanni, A.; Salem, H.; Tagel-Din, H. Applied Element Method Analysis of Porous GFRP Barrier Subjected to Blast. *Adv. Struct. Eng.* **2010**, *13*, 153–169. [CrossRef]
32. Zhou, P.; Bazargan, M.; Lanaro, F.; Shirzadegan, S.; Nikadat, N.; Warema, S.; Malmgren, L.; Sjoberg, J.; Nordlund, E. Dynamic modelling of rock bolts at Kiirunavaara mine. *Int. J. Rock Mech. Min. Sci.* **2024**, *178*, 105753. [CrossRef]
33. Li, F.; Quan, X.; Jia, Y.; Wang, B.; Zhang, G.; Chen, S. The Experimental Study of the Temperature Effect on the Interfacial Properties of Fully Grouted Rock Bolt. *Appl. Sci.* **2017**, *7*, 327. [CrossRef]
34. Sun, Z.; Zhang, D.; Fang, Q.; Liu, D.; Dui, G. Displacement process analysis of deep tunnels with grouted rockbolts considering bolt installation time and bolt length. *Comput. Geotech.* **2021**, *140*, 104437. [CrossRef]
35. Zekavati, M. Finite element modeling of the influence of FRP techniques on the seismic behavior of an arch stone bridge of historical interest. *Insight Civil Eng.* **2024**, *7*, 619. [CrossRef]
36. Wu, Z.X.; Lei, J.J.; Ye, C.P.; Yu, C.; Zhao, J.L. Coupled FDM-DEM simulations of axial compression tests on FRP-confined concrete specimens. *Constr. Build. Mater.* **2022**, *351*, 128885. [CrossRef]

https://doi.org/10.3390/infrastructures11030100